



Mass extinction spectra and size distribution measurements of quartz and amorphous silica aerosol at 0.33–19 μm compared to modelled extinction using Mie, CDE, and T -matrix theories



Benjamin E. Reed^{a,*}, Daniel M. Peters^{a,b}, Robert McPheat^b, Andrew J.A. Smith^c, R.G. Grainger^d

^a Atmospheric, Oceanic and Planetary Physics, University of Oxford, Oxford, OX1 3PU, U.K.

^b RAL Space, STFC Rutherford Appleton Lab, Harwell, OX11 0QX, U.K.

^c National Centre for Earth Observation, Atmospheric, Oceanic and Planetary Physics, University of Oxford, Parks Road, Oxford OX1 3PU, U.K.

^d COMET, Atmospheric, Oceanic and Planetary Physics, University of Oxford, Parks Road, Oxford, OX1 3PU, U.K.

ARTICLE INFO

Article history:

Received 23 March 2017

Revised 11 May 2017

Accepted 11 May 2017

Available online 19 May 2017

Keywords:

Mass extinction coefficient

Aerosols

Quartz

Amorphous silica

Mie theory

Non-spherical scattering

T -matrix theory

Rayleigh CDE model

ABSTRACT

Simultaneous measurements were made of the spectral extinction (from 0.33–19 μm) and particle size distribution of silica aerosol dispersed in nitrogen gas. Two optical systems were used to measure the extinction spectra over a wide spectral range: a Fourier transform spectrometer in the infrared and two diffraction grating spectrometers covering visible and ultraviolet wavelengths. The particle size distribution was measured using a scanning mobility particle sizer and an optical particle counter. The measurements were applied to one amorphous and two crystalline silica (quartz) samples. In the infrared peak values of the mass extinction coefficient (MEC) of the crystalline samples were $1.63 \pm 0.23 \text{ m}^2\text{g}^{-1}$ at 9.06 μm and $1.53 \pm 0.26 \text{ m}^2\text{g}^{-1}$ at 9.14 μm with corresponding effective radii of 0.267 and 0.331 μm , respectively. For the amorphous sample the peak MEC value was $1.37 \pm 0.18 \text{ m}^2\text{g}^{-1}$ at 8.98 μm and the effective radius of the particles was 0.374 μm . Using the measured size distribution and literature values of the complex refractive index as inputs, three scattering models were evaluated for modelling the extinction: Mie theory, the Rayleigh continuous distribution of ellipsoids (CDE) model, and T -matrix modelling of a distribution of spheroids. Mie theory provided poor fits to the infrared extinction of quartz ($R^2 < 0.19$), although the discrepancies were significantly lower for Mie theory and the amorphous silica sample ($R^2 = 0.86$). The CDE model provided improved fits in the infrared compared to Mie theory, with $R^2 > 0.82$ for crystalline silica and $R^2 = 0.98$ for amorphous silica. The T -matrix approach was able to fit the amorphous infrared extinction data with an R^2 value of 0.995. Allowing for the possibility of reduced crystallinity in the milled crystal samples, using a mixture of amorphous and crystalline T -matrix cross-sections provided fits with R^2 values greater than 0.97 for the infrared extinction of the crystalline samples.

© 2017 The Authors. Published by Elsevier Ltd.

This is an open access article under the CC BY license. (<http://creativecommons.org/licenses/by/4.0/>)

1. Introduction

Atmospheric aerosols directly affect the Earth's radiative balance, across the electromagnetic spectrum from the infrared (IR) to the ultraviolet (UV), by scattering and absorbing solar radiation as well as absorbing and emitting infrared radiation [1,2]. Atmospheric aerosols also affect the climate indirectly by acting as ice and cloud condensation nuclei [3,4] and by providing catalytic surfaces for heterogeneous chemical reactions [5]. Uncertainties in

quantifying the direct and indirect effects of aerosols on radiative forcing are two of the largest contributions to the uncertainty in predicting future climate change [6].

Atmospheric mineral dust has a significant impact on the Earth's climate [6]. Between 1000–3000 Mt of wind blown dust enters the atmosphere annually [7], largely from arid and semi-arid regions located in a broad band that stretches from the west coast of North Africa, through the Middle East, to Central Asia [8]. The Sahara is the largest emission source, at an estimated 670 Mt yr⁻¹, generating the largest atmospheric mass loading of mineral dust aerosol [9]. Strong winds and convection from surface heating uplift mineral dust particles into the troposphere, at

* Corresponding author.

E-mail address: benjamin.reed@physics.ox.ac.uk (B.E. Reed).

which point atmospheric circulation can transport the dust on intercontinental scales [10–13], reaching as far as Northern Europe and South America [14,15].

Silicon dioxide (silica) is the most abundant oxide in the Earth's crust comprising an estimated 12% by volume [16]. Naturally occurring silica is found in the form of crystalline alpha-quartz which has a regular structure of SiO_4 tetrahedra. Quartz is a major externally mixed constituent of wind blown mineral dust, although its percentage by mass in atmospheric dust samples has been found to vary significantly by location [17,18].

Silica is also a major internally mixed constituent of volcanic ash, which has silica content varying from 50–75% [19,20]. Even moderately sized volcanic eruptions can inject many hundreds of megatonnes of volcanic ash into the troposphere and stratosphere, following which the plume can be transported thousands of kilometres posing significant risk to aviation [21–23]. The 2010 Eyjafjallajökull volcanic eruption injected approximately 380 Mt of ash into the atmosphere [24] and is estimated to have cost the global economy US \$ 5 bn [25,26] resulting from six days of European airspace closure as the ash plume propagated downwind. The silica within volcanic ash is mainly quenched into fragments of amorphous volcanic glass, which consists of disordered networks of SiO_4 tetrahedra interconnected with other minerals [27]. The strong infrared absorption feature of volcanic ash at 8–12 μm , attributable to T–O[−] vibrations (where T indicates fourfold coordinated cations, predominately Si^{4+} , Al^{4+} and Fe^{3+}) [28], is widely exploited for rapid ash detection using satellites and other remote sensing instruments [29,30]. For example, large negative brightness temperature differences between 10 and 12 μm channels are used by nadir imaging instruments to indicate the presence of ash [31].

The scattering and absorption of radiation produced by aerosol particles depend on the particles' size distribution, complex refractive index and shape distribution [32]. A large component of the uncertainty in modelling the effect of aerosols on atmospheric radiative transfer comes from uncertainty in assumptions about these parameters and the untangling of their individual effect on bulk optical properties such as the volume extinction coefficient and phase function; these uncertainties propagate to uncertainties in remote sensing of aerosols and radiative forcing calculations [33–35].

A scattering theory is required to determine the bulk optical properties from the size distribution, complex refractive index and shape distribution of the particles. In many applications the particles are assumed to be spheres, and Mie theory is used. The extinction produced by irregularly shaped mineral dust particles, including near to their infrared absorption features, is not well modelled by assuming spheres [36]. Significant errors are introduced when Mie scattering is assumed for remote sensing retrievals and climate forcing calculations [37,38]. In the Rayleigh approximation, simple analytic expressions can be derived for the scattering and extinction cross sections of randomly oriented idealized particle shapes (such as disks, needles and ellipsoids). The extinction predicted by assuming a continuous distribution of ellipsoids (CDE), in which all geometric shape factors are equally probable, provides a much improved fit to the infrared extinction of silica particles than Mie theory [32].

Substantial theoretical progress has been made in modelling the light scattering of non-spherical atmospheric aerosols. The discrete dipole approximation [39,40] and the finite difference time domain [41,42] methods have been applied to non-spherical, inhomogeneous particles. However, these techniques are highly computationally expensive, limiting their applicability to relatively small particles. *T*-matrix methods are widely used to model the scattering of irregularly shaped atmospheric aerosols [43,44]. The spheroid approximation is commonly applied within the *T*-matrix

calculations because the orientational averaging is greatly simplified, reducing computational expense. The spheroid approach has been shown to provide more flexibility in matching the scattering of mineral dust compared to polyhedral prisms, and performs well compared to many other scattering models at matching light scattering data [45]. *T*-matrix methods, using a distribution of spheroids, have been applied to model climate forcing and within mineral dust remote sensing retrievals [46–48].

Despite the importance of the optical properties of solid atmospheric aerosol particles there are relatively few experimental measurements of these properties over the full spectrum relevant to atmospheric radiative transfer. This paper details a newly developed experimental technique and apparatus capable of accurately measuring the spectral extinction and size distribution of solid aerosol particles suspended in nitrogen gas. Two optical systems were used, covering wavelengths from the UV through to the IR (0.33–19 μm) and providing high spectral resolution (1.9 cm^{-1} in the IR and < 1.5 nm in the shortwave). Simultaneously, the size distribution of particles was measured and filter samples suitable for scanning electron microscope (SEM) imaging were taken, allowing a full microphysical analysis of the particles. Previous high-quality laboratory measurements of the spectral extinction and size distribution of solid aerosol particles have been performed by [49–51]. These earlier measurements were limited to infrared wavelengths and were performed at the lower resolution of 8 cm^{-1} . Previous broadband extinction measurements of quartz aerosol have been performed by [52], however the particles' size distribution was not measured concurrently in this work.

This paper presents measurements applied to three high purity silica samples. The experimental apparatus and method have been significantly adapted from previous experiments on black carbon, presented in [53]. The motivation for the silica measurements is twofold. Firstly, silica is a major component of mineral dust and volcanic ash, both of which are important atmospheric aerosols. Secondly, the complex refractive indices of amorphous and crystalline silica are well documented in the literature, allowing the experimental extinction data to be evaluated against various scattering models (using the measured size distribution as an input), and allowing an assessment of the accuracy of the experimental method.

The paper is organised as follows. In Section 2 the experimental method and apparatus are outlined, and details about the three silica samples are provided. In Section 3 the analysis of the experimental data is detailed and results for the size distribution and the spectral mass extinction coefficient, with uncertainty, of the samples are presented. In Section 4, three scattering models – Mie theory, the Rayleigh CDE model, and *T*-matrix methods applying a distribution of spheroids are described. The modelled extinction using each theory, taking literature values of the complex refractive index of silica and the measured size distribution as inputs, are compared to the experimental extinction data. In Section 5 conclusions and planned future work are described.

2. Method

2.1. Overview of experimental setup

Experiments were performed at Rutherford Appleton Laboratory's Molecular Spectroscopy Facility (RAL-MSF). The samples were dispersed in nitrogen gas and passed into a 75 l aerosol cell chamber; the aerosol cell has been described in detail in [54]. Inside the cell, the optical extinction of the aerosol was measured at infrared wavelengths using a Fourier transform spectrometer, concurrent to ultraviolet and visible (VIS) extinction measurements made by two diffraction grating spectrometers. Upon leaving the cell, the size distribution of particles was measured by a scanning

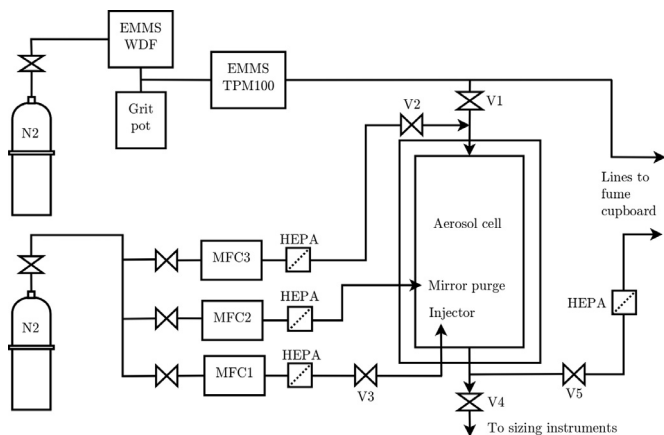


Fig. 1. The experimental apparatus used to supply the aerosol cell with a near-constant number density of dispersed aerosol. The abbreviations are as follows. HEPA – high-efficiency particulate arrestance filter. EMMS – Electro-Medical Measurements Systems. WDF – Wright dust feeder. TPM – total particulate monitoring system. MFC – mass flow controller. V – valve.

mobility particle sizer (SMPS), covering particle radii in the range $0.005 < r < 0.44 \mu\text{m}$ using 44 logarithmically spaced size bins, and an optical particle counter (OPC), covering $0.15 < r < 10 \mu\text{m}$ using 14 logarithmically spaced size bins.

2.2. Aerosol dispersal and flow configuration

Fig. 1 shows the apparatus used to supply a near-constant number density of dispersed aerosol to the cell. The samples were dried for several hours at 90°C to remove any moisture and were compacted into the Wright dust feeder (WDF) sample cup using a hydraulic press. The samples were dispersed using the WDF manufactured by Electro-Medical Measurement Systems (EMMS). A Peak Scientific generator supplied nitrogen gas to the WDF. The WDF used a rotating blade to remove a thin layer from the surface of the compacted sample which is added to the gas flow. A Venturi tube within the WDF acted to separate the sample into individual particles. After passing vertically down through the Venturi the flow passed a 90° bend to the horizontal, removing $> 80\%$ particles larger than $10 \mu\text{m}$ into a grit pot.¹ The EMMS total particulate monitoring transducer (TPM) was used to monitor output from the WDF and once a steady rate of aerosol was observed the aerosol was passed into the aerosol cell by opening valve V1.

Three mass flow controllers (MFCs) provided additional nitrogen gas to the cell. MFC3 allowed additional aerosol dilution. MFC2 provided a constant purge to the cell windows and optical mirrors, preventing aerosol contamination. MFC1 controlled a turbulent jet flow used to ensure uniform aerosol mixing within the cell.

During experiments, once the TPM observed a constant WDF output, valves V1–V4 would be open and valve V5 closed. All other valves shown in **Fig. 1** were open. The total flow provided by MFC1–MFC3 was less than the WDF flow ensuring the aerosol flow passed through valve V1 and exited through valve V4. The optical and sizing instruments were set to make continuous repeat measurements throughout the experiment. Once the experiment was complete the cell was completely purged of aerosol by closing valves V1 and V4, opening valve V5 and increasing the flows provided by MFC1–MFC3 so that remaining aerosol exited via valve V5 to a fume cupboard.

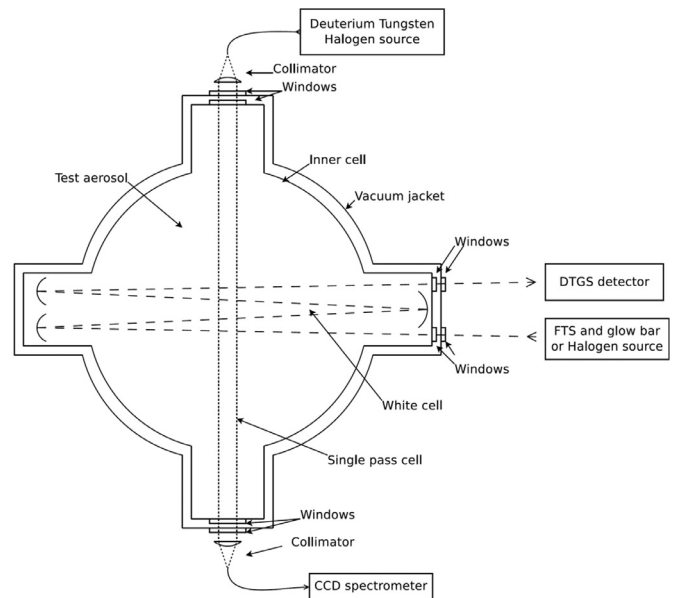


Fig. 2. The optical setup within the aerosol cell. The abbreviations are defined as follows. CCD – charge coupled device. FTS – Fourier transform spectrometer. DTGS – deuterated triglycine sulphate detector.

2.3. Optical measurements

The aerosol extinction was measured using two separate optical systems within the cell. **Fig. 2** shows a horizontal cross section of the cell and demonstrates the two systems.

Measurements in the IR were made using a Bruker Vertex 80V FTS operating at a resolution of 1.9 cm^{-1} . The FTS alternated between two sources: a globar (GB) and a halogen lamp (HL). The FTS modulated the light before passing it into the cell; the returning light was measured using a deuterated triglycine sulphate detector. The GB working range was approximately $526\text{--}5000 \text{ cm}^{-1}$ ($19\text{--}2.0 \mu\text{m}$), and the HL range was $667\text{--}8000 \text{ cm}^{-1}$ ($15\text{--}1.25 \mu\text{m}$). A White cell [56], consisting of three spherical concave mirrors, with eight optical passes was used within the cell to increase the optical path to 3.52 m, allowing increased sensitivity to low concentrations of aerosol. During experiments the FTS continuously measured the light transmitted through the cell, alternating between the GB and the HL source. Each FTS measurement took approximately one minute and comprised 68 complete scans of the interferometer's moving mirror. There were four minutes between successive GB or HL measurements, because of the time taken to switch between sources and complete the interferometer's mirror scans.

In the UV and VIS a deuterium tungsten halogen source was coupled to a collimator and the light was sent on a single pass through the cell. The optical path was 0.427 m, perpendicular to the IR measurements. Light transmitted through the cell was focused (using a lens with a focal length of 100 mm) into a bifurcated optical fibre (with a diameter of $600 \mu\text{m}$) which split the beam into optical fibres passing to two Ocean Optics S2000 CCD diffraction grating spectrometers. The angle of acceptance of the measurements was 0.35° , meaning the effect of forward scattering contamination was negligible. One spectrometer was configured to make measurements covering $200\text{--}850 \text{ nm}$ at a resolution of 1.33 nm , whilst the second covered $530\text{--}1100 \text{ nm}$ with a resolution of 1.17 nm . Both spectrometers were wavelength-calibrated to within 1 nm . During experiments the spectrometers made measurements continuously at intervals of 20 s .

¹ Estimated using the Particle Loss Calculator [55].

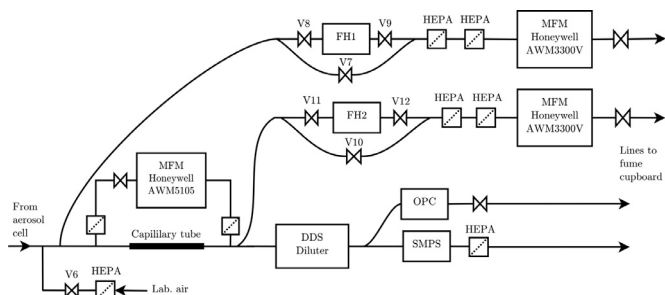


Fig. 3. Aerosol sizing and sampling. FH – filter holder. MFM – mass flow meter. DDS – Dynamic Dilution System. OPC – optical particle counter. SMPS – scanning mobility particle sizer.

2.4. Sizing and filter measurements

After leaving the cell the aerosol passed to a suite of sizing and sampling instruments, shown in Fig. 3. The size distribution of the aerosol was measured using an SMPS, consisting of a Grimm 5.5–900 differential mobility analyser and Grimm 5403 Ultrafine Particle Counter, and a Grimm 1.108 OPC.

Before passing to the OPC and SMPS, the aerosol flow passed two stages of dilution. A capillary tube connected in parallel to a Honeywell AWM5105 MFM provided a dilution of approximately 5: 1, and the Model 560 Dynamic Dilution System (DDS), manufactured by Topas GmbH, provided further dilution of 20: 1, giving a combined dilution at the SMPS and OPC compared to the cell of approximately 100: 1. This level of dilution was required to reduce particle concentrations to levels that could be accepted by the SMPS and OPC. The precise level of dilution was determined from the size distribution returned by the instruments and a mass loading filter sample measurement made within filter holder 1 (FH1).

Two simultaneous filter samples, at different levels of dilution, were taken for each experiment. FH1 was loaded with a Merck Millipore 47 mm diameter polycarbonate filter, which had pores of radius 0.05 μm. This filter sampled aerosol directly (without dilution) from the cell. The gas flow rate through the filter was recorded continuously using a Honeywell AWM3300 V mass flow meter (MFM). The mass of the filter was measured before the experiment using a micro-balance accurate to 0.0001 g. The aerosol number density within the cell reached a steady equilibrium approximately 15 min after valve V1 was opened and aerosol was drawn into the cell; determined by monitoring for a constant cell input number density measured by the TPM and cell output number densities measured by the sizing instruments. Once a near-constant number density in the cell was attained, the filter exposure was started by opening valves V8 and V9 and closing valve V7. The filters used a bypass system so that the flow remained constant, e.g. whenever filter valves V8 and V9 were closed valve V7 would be open and vice versa. The start and end times of the exposure were recorded and filters were exposed for 60 min or until the sample ran out. The mass of the loaded filter was then measured, so that the initial filter mass could be subtracted to determine the aerosol loading mass.

FH2 contained a Merck Millipore 47 mm polytetrafluoroethylene filter, and sampled the aerosol flow after the first level of dilution. These filter samples were suitable for scanning electron microscope imaging.

2.5. The samples

Three powdered silica samples were tested. Sample A was crystalline alpha-quartz with product name 'Crystalite 5X' supplied by Tatsumori Ltd (Lot 3H-3110). The sample had a quoted SiO₂ pu-

rity of > 99.8 % and a quoted mass-weighted mean particle radius of 0.55 μm. Sample B was crystalline alpha-quartz supplied by The Quartz Corp (Lot 2154) and had a quoted purity of > 99.99 %. Sample C was amorphous silica with product name 'Fuselex WX' supplied by Tatsumori Ltd (Lot 2K-3201) with a quoted SiO₂ purity of > 99.98 % and a mass-weighted mean radius of 0.55 μm. All three samples were milled by their manufacturers to produce the fine particle powders. The amorphous sample was produced from natural quartz through the application of heat followed by milling.

3. Analysis and results

3.1. Radiance to mass extinction

The aerosol transmittance, $T(\lambda)$, was determined from measuring background radiance spectra when the cell was empty, $L_b(\lambda)$, and measurement radiance spectra when the cell contained aerosol, $L_m(\lambda)$. The aerosol transmittance is related to the volume extinction coefficient, β^{ext} (units: m⁻¹), according to:

$$\frac{L_m(\lambda)}{L_b(\lambda)} = T(\lambda) = \exp(-\beta^{\text{ext}}(\lambda)x), \quad (1)$$

where x is the path length of the optical system ($x = 3.52$ m for the FTS measurements and $x = 0.427$ m for the shortwave system). The mass extinction coefficient (MEC), k^{ext} (units: m²g⁻¹), is defined as:

$$k^{\text{ext}}(\lambda) = \frac{\beta^{\text{ext}}(\lambda)}{\rho_a}, \quad (2)$$

where ρ_a is the mass of aerosol per unit volume.

Background radiance measurements were made by measuring the empty cell for 30 minutes immediately before experiments and for 30 minutes after the cell had been completely purged of aerosol. The value of L_b could then be calculated by linearly interpolating the before and after background measurements to the time of each aerosol measurement, in this way correcting for the possibility of drift in the source radiance. The background drift was < 1 % in all cases. The aerosol transmittance was calculated as the mean of the repeated transmittance measurements over the filter exposure period.

For the Ocean Optics shortwave measurements, 20 min of dark current measurements were made with the spectrometer's shutter closed immediately before background measurements were performed. The dark current was then subtracted from both measurement and background radiances, before transmittance was calculated according to Eq. (1).

The uncertainty in the mean radiance measurements at each wavelength, $\sigma_{\text{mean}}(\lambda)$, taking into account auto-correlation between successive measurements, was calculated according to the formula detailed in [57]:

$$\sigma_{\text{mean}}(\lambda) = \frac{\sigma(\lambda)}{\sqrt{N}} \times \left[\frac{1 + w(\lambda)}{1 - w(\lambda)} \right], \quad (3)$$

where $\sigma(\lambda)$ is the unbiased standard deviation of radiance measurements at wavelength λ over the time period for which the mean was calculated, N is the number of radiance measurements during this period, and $w(\lambda)$ is the Prais–Winsten estimate of the auto-correlation. In spectral regions where the radiance measurements from different instruments overlapped, the measurements were interpolated to a common grid and the uncertainty-weighted mean was calculated. Uncertainties were propagated, using standard methods, to all subsequently derived quantities, and where these calculations included other measured quantities (e.g. ρ_a in Eq. (2)) the associated uncertainties were combined using standard error propagation formulae [58].

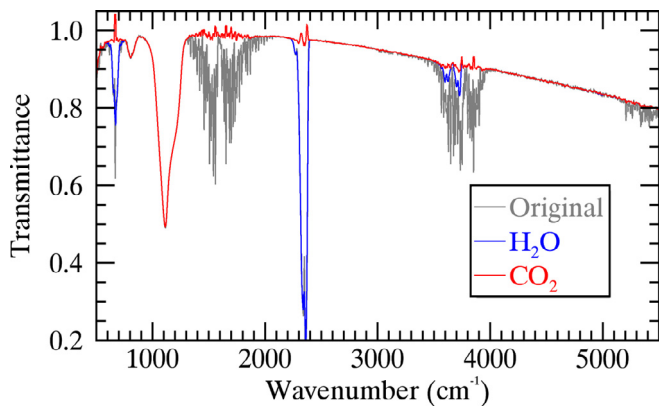


Fig. 4. Gas removal from the mean transmittance measurement of Sample C made by the FTS with the GB source. The grey line shows the original spectrum, the blue-coloured curve shows the spectrum with H₂O gas lines removed and the red-coloured curve shows the spectrum with both H₂O and CO₂ lines removed. (For interpretation of the references to colour in this figure legend, the reader is referred to the web version of this article.)

3.2. Removal of gas absorption lines and the in-cell relative humidity

The Peak Scientific generator did not provide 100% pure nitrogen and contaminating H₂O and CO₂ lines were present in both L_b and L_m. The method detailed in [53] was used to retrieve the concentrations of these gases from the measured transmissions spectra, allowing the aerosol transmittance to be separated from the gas absorption transmittance. The measured transmittance can be expressed as:

$$T(\lambda) = T_g(\lambda) \times T_a(\lambda), \quad (4)$$

where T_a is the aerosol transmittance and T_g is the gas transmittance. The aerosol transmittance can be assumed to vary smoothly over tens of wavenumbers, whereas rapid spikes in transmittance can be attributed to gas absorption. The ratio of the measured transmittance to the measured transmittance with a boxcar smoother applied was calculated. The same quantity was modelled using the Reference Forward Model [59] taking into account the instrument lineshape function. The Levenberg–Marquardt method, detailed in [60], was used to search for the concentration of gases that best fitted the data. Fig. 4 shows an example of gas line removal from the FTS measurement of Sample C made using the GB source. The gas retrieval was first performed for H₂O in the wavenumber (ν) region $1400 < \nu < 2000 \text{ cm}^{-1}$, where there are strong H₂O lines and no CO₂ lines. The blue-coloured curve in Fig. 4 shows the spectra after H₂O lines have been removed. The gas retrieval was then performed for CO₂ in the region $2250 < \nu < 2450 \text{ cm}^{-1}$, and the red-coloured curve in Fig. 4 shows the spectrum after both H₂O and CO₂ lines have been removed.

The gas line retrieval returned the concentration of water vapour, $x_{\text{H}_2\text{O}}$, in parts per million by volume, which is related to the in-cell relative humidity, RH, according to:

$$\text{RH} = x_{\text{H}_2\text{O}} \times 10^{-6} \times \frac{P}{e_s}, \quad (5)$$

where P is the total pressure and e_s is the saturation vapour pressure of water. The total pressure was monitored during experiments using an in-cell pressure meter, and e_s was calculated according to the equation given in [61].

3.3. Dilution calibration and in-cell size distribution results

The aerosol flow passed through two stages of dilution before reaching the sizing instruments. It was necessary to precisely determine the total dilution factor, D , between the cell and the siz-

ing instruments. The direct mass loading measurement made using FH1 was used for this purpose. The in-cell aerosol mass per unit volume, ρ_a , could be calculated from the deposited filter mass, M_{FH1} , according to:

$$\rho_a = M_{\text{FH1}} \times Q_{\text{FH1}} \times t_{\text{FH1}} \quad (6)$$

where Q_{FH1} was the mean flow rate passing through FH1 measured continuously by the mass flow meter (the flow rate varied by less than 1% throughout experiments) and t_{FH1} was the filter exposure time period.

The SMPS measures the electrical mobility radius, r_{em} , of particles which is related to the volume equivalent radius, r_{ve} , according to the equation detailed in [62]:

$$\frac{r_{\text{em}}}{C_s(r_{\text{em}})} = \frac{r_{\text{ve}} \chi}{C_s(r_{\text{ve}})} \quad (7)$$

where the volume equivalent radius, r_{ve} , is defined as the radius of a particle having the same volume as the non-spherical particle under consideration; $C_s(r)$ is the Cunningham slip correction, for which the parameterisation found by [63] was assumed, and χ is the dynamic shape factor of particles, which was assumed to have a value $\chi = 1.0$ consistent with the result found by [51] for similarly sized quartz particles. The electrical mobility radius returned by the SMPS was corrected to the volume equivalent radius, according to Eq. (7) allowing comparison with the OPC measurements.

The Grimm 1.108 OPC measures the integrated scattered intensity (over scattering angles $\Theta = 30\text{--}150^\circ$) of individual particles passing through a 780 nm laser beam and uses the instrument's response curve to assign the particle to a radius bin. The response curve of the instrument assumed Mie scattering and a complex refractive index of $m = 1.60 + 0.0i$. Literature values for the complex refractive index of crystalline and amorphous silica [64,65] were used to calculate a corrected Mie response curve of the instrument from which corrected bin radii were determined; the correction to bin radius was less than 10% for all bins.

Once the SMPS data had been converted to volume equivalent radius and the OPC data had been corrected for refractive index, mean size distributions were calculated for each instrument. The mean was calculated for distributions measured during the filter exposure time period. The SMPS and OPC mean distributions were combined by using SMPS data up to its largest radius bin and OPC data for larger radii thereafter. The combined at-instrument (AI) size distribution, $(dN/d\ln r)_{\text{AI}}$ where N has units of particles per cm³, was then used to calculate the dilution factor, D , according to:

$$D = \frac{\rho_a}{\rho_p \int_{r=0.05\mu\text{m}}^{\infty} \frac{4}{3} \pi r^3 \left(\frac{dN}{d\ln r} \right)_{\text{AI}} d\ln r} \quad (8)$$

where ρ_p was the particle density ($\rho_p = 2.65$ and 2.20 g cm^{-3} for crystalline and amorphous silica, respectively). The denominator of Eq. (8) represents the mass per unit volume at the sizing instruments for the fraction of particles with radii larger than $0.05\mu\text{m}$. The filter had a pore radius of $0.05\mu\text{m}$ and it was assumed that only particles with $r \geq 0.05\mu\text{m}$ were collected (by mass the finer fraction was significantly less than 1%). The in-cell size distribution was given by:

$$\left(\frac{dN}{d\ln r} \right)_{\text{cell}} = D \times \left(\frac{dN}{d\ln r} \right)_{\text{AI}} \quad (9)$$

Fig. 5 shows the results for the in-cell size distributions measured for the three silica samples. The plots show data from both the SMPS and the OPC, multiplied by the dilution factor calculated according to Eq. (8). There is good agreement between the two instruments in the overlap region, and in-cell particle number densities were similar between the three experiments indicating the

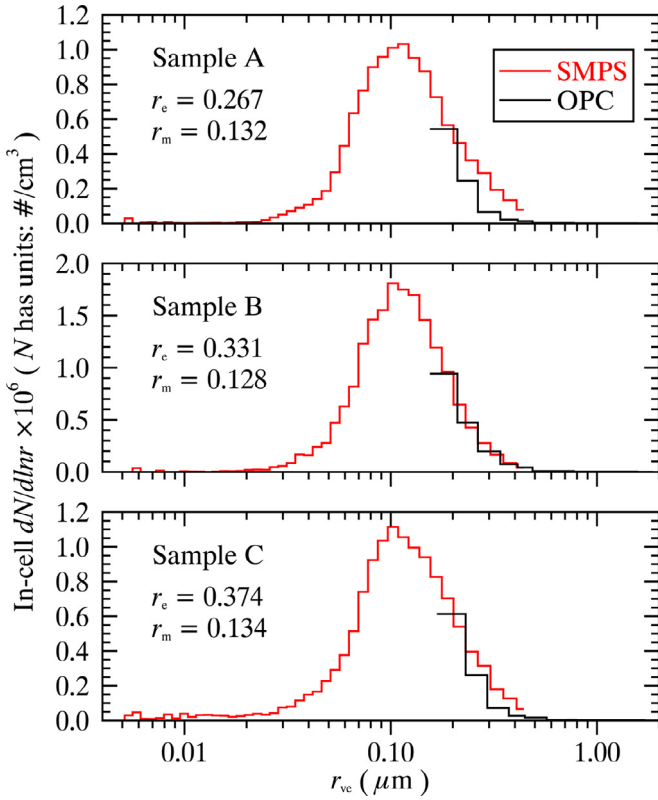


Fig. 5. The in-cell size distributions of the three samples. The SMPS and OPC in-instrument size distributions were multiplied by the dilution factor, D .

Table 1

Lognormal parameters describing fits to the in-cell size distributions.

Sample	N_0 ($\times 10^6$ cm $^{-3}$)	r_0 (μ m)	S
A	1.404	0.1139	1.694
B	1.852	0.1128	1.595
C	1.493	0.1181	1.700

WDF provided good repeatability. Values are also given in the figure for the effective radius, r_e , and the mean radius, r_m , calculated for each combined distribution. The number weighted mean standard error in $dN/dlnr$ across the radius bins was approximately 10 % for the SMPS and 1 % for the OPC, with little variation in values between the samples.

Lognormal distributions were fitted to the measured size distributions. The fitted parameters are detailed in Table 1. The lognormal distribution is defined according to:

$$\frac{dN}{d \ln r} = \frac{N_0}{\sqrt{2\pi} \ln(S)} \exp \left[-\frac{(\ln r - \ln r_0)^2}{2 \ln^2(S)} \right], \quad (10)$$

where N_0 is the total number of particles per unit volume, r_0 is the median particle radius, and S is the geometric standard deviation.

3.4. Mass extinction coefficient results and in-cell parameters

Fig. 6 shows the spectral mass extinction coefficient, $k^{\text{ext}}(\lambda)$, results for the three silica samples. Table 2 shows results for the in-cell gas concentrations and relative humidity; it is important to quote relative humidity with extinction measurements because it is known to affect aerosol scattering properties [66]. The extinction curves generally show a decrease of extinction with wavelength. This trend is punctuated by regions of high extinction generated by the loss of energy associated with vibrational bands. The de-

Table 2

In-cell gas concentrations and relative humidity.

Sample	CO $_2$ (PPMV)	H $_2$ O (PPMV)	RH (%)
A	227.0 \pm 2.4	403.4 \pm 3.5	0.163 \pm 0.001
B	329.4 \pm 1.5	1019.5 \pm 5.2	0.411 \pm 0.002
C	240.0 \pm 1.0	913.9 \pm 3.4	0.369 \pm 0.001

creasing trend is caused by the reduction in scattering efficiency as the particle size becomes smaller than the wavelength of the incident light.

There are two clear absorption features at approximately 9 and 12.5 μ m in the extinction spectra of both the crystalline samples and the amorphous sample. The feature at \sim 9 μ m is associated with the asymmetric stretching vibrations of Si–O–Si bridges and the \sim 12.5 μ m feature is associated with symmetric vibrations involving displacement of the O atom perpendicular to the Si–Si direction in the Si–O–Si plane [67,68].

Comparing the extinction spectra of the two crystalline samples, Sample A and Sample B, the shape of the curves in the infrared are similar. However, the Si–O–Si asymmetric stretching feature of Sample A has a slightly higher peak value and the feature is narrower than the same feature in Sample B; the peak MEC value for Sample A is 1.63 ± 0.23 m 2 g $^{-1}$ at 9.06 μ m and for sample B the peak value is 1.53 ± 0.26 m 2 g $^{-1}$ at 9.14 μ m. Both crystalline samples show a distinct local maximum and minimum to the left of the main asymmetric stretching peak at approximately 8.6 μ m. The symmetric stretching features at 12.5 μ m show similar shapes, however for Sample B the feature is broader and slightly higher. The differences in the infrared extinction spectra of the two crystalline samples may reflect differences in the complex refractive index of the samples, the shape of particles, or the particle size distribution. Differences in the complex refractive index may derive from impurities. However, due to the high purity of the samples differences in the crystalline character of the fine particles are likely to have had a more significant effect on refractive index. Fine particles may lose the regular crystal structure of the bulk material from which they were derived, showing increased disorder and amorphous character [69–71]. The infrared absorption features of the amorphous sample (Sample C) appear as a smoothed version of the crystalline features. The Si–O–Si asymmetric vibration feature does not show the local maximum at about 8.6 μ m that is present for the crystalline samples. The peak is lower than both crystalline samples with a MEC value of 1.37 ± 0.18 m 2 g $^{-1}$ occurring at 8.98 μ m (blue shifted relative to the crystalline samples). Similarly, the feature at 12.5 μ m is much flatter and does not have the distinct double peak signature of the crystalline samples.

4. Theoretical modelling of extinction spectra

4.1. The scattering models

Three scattering models were investigated for modelling the spectral extinction of silica aerosol: Mie theory, the continuous distribution of ellipsoids (CDE) model, and T -matrix methods applying a discrete distribution of spheroids. In all cases, the volume extinction coefficient can be expressed as:

$$\beta^{\text{ext}} = \int_0^\infty \sigma^{\text{ext}} n(r) dr, \quad (11)$$

where $n(r) = dN/dr$ is the number of particles per unit volume with radii between r and $r + dr$ and σ^{ext} is the extinction cross section which, in general, is a function of the complex refractive index, $m(\lambda) = n + ik$, the particle size parameter, $x = 2\pi r/\lambda$, and the particle shape. In the case of non-spherical particles the size parameter is typically expressed in terms of the volume equivalent

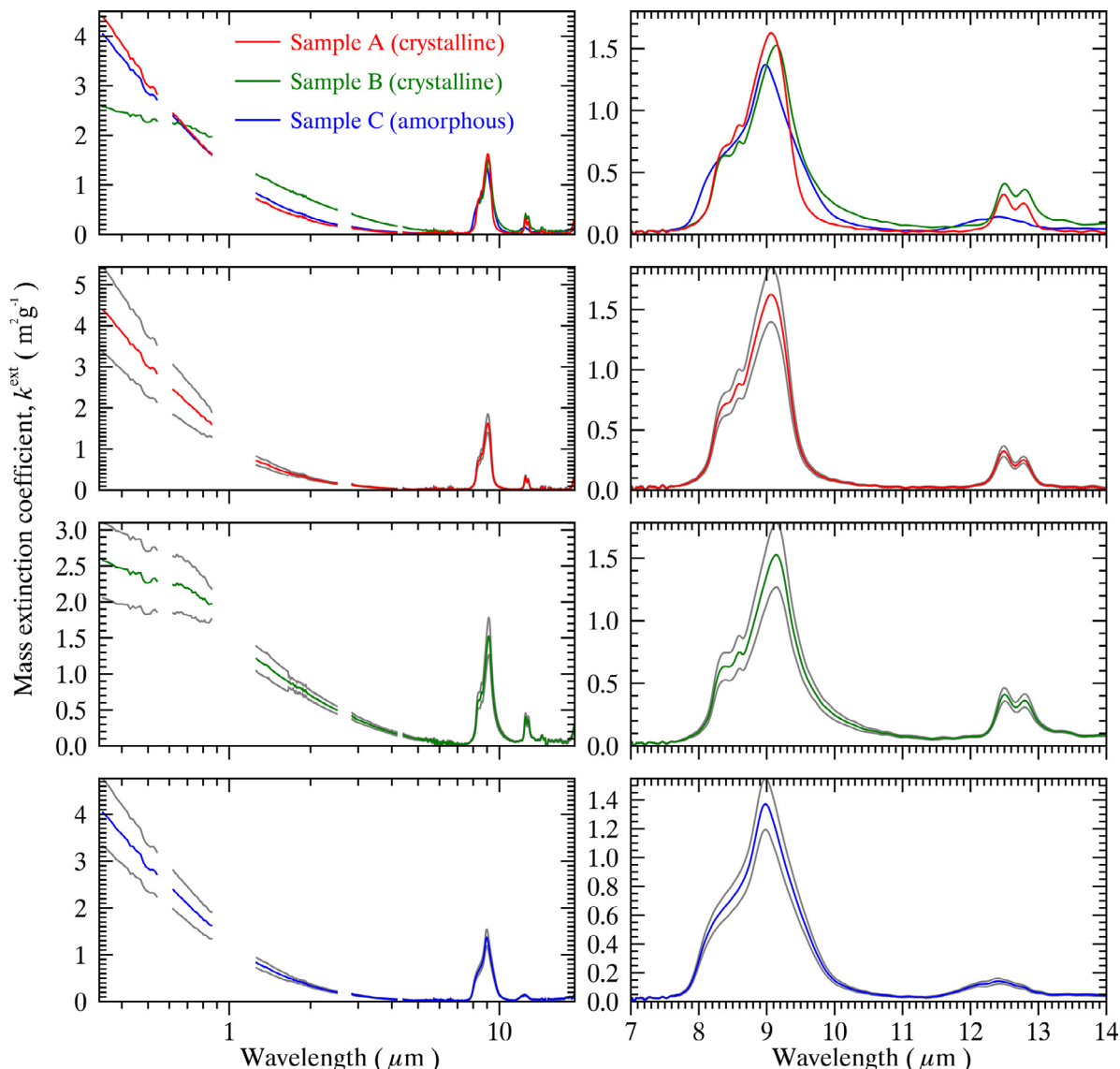


Fig. 6. The spectral mass extinction coefficients, $k^{\text{ext}}(\lambda)$, of the three silicon dioxide samples. The first row shows all three samples over-plotted, whilst the lower rows show individual results with one-sigma uncertainty (shown in grey). The first column of plots shows MEC over the full spectral range, 0.33–19 μm , with a logarithmic wavelength scale, whilst the second column shows MEC in the range 7–14 μm with a linear scale.

radius, r_{ve} , defined as the radius of an equivalent sphere having the same volume as the particle under consideration. The extinction cross section can be expressed in terms of the absorption and scattering cross sections:

$$\sigma^{\text{ext}} = \sigma^{\text{sca}} + \sigma^{\text{abs}}. \quad (12)$$

Mie theory describes the exact solution to the electromagnetic scattering and absorption produced by a sphere. The Mie extinction cross section is expressed in terms of the infinite series:

$$\sigma_{\text{Mie}}^{\text{ext}} = \frac{\lambda^2}{2\pi} \sum_{n=0}^{\infty} (2n+1) \text{Re}[a_n(m, x) + b_n(m, x)], \quad (13)$$

where $a_n(m, x)$ and $b_n(m, x)$ are the scattering coefficients which depend on the complex refractive index and the size parameter, and are expressed in terms of the Riccati-Bessel functions. The code used to evaluate the solution numerically is similar to that detailed in [32], and can be found at: http://eodg.atm.ox.ac.uk/MIE/mie_single.html.

In the Rayleigh approximation ($x \ll 1$), it can be shown that the absorption and scattering cross sections for a continuous distribu-

tion of ellipsoids (CDE), in which all shapes are equally probable, can be expressed as [32,72]:

$$\sigma_{\text{CDE}}^{\text{abs}} = kV \text{Im} \left[\frac{2m^2}{m^2 - 1} \ln(m^2) \right], \quad (14)$$

$$\sigma_{\text{CDE}}^{\text{sca}} = \frac{k^4 V^2 |m^2 - 1|^2}{3\pi \text{Im}(m^2)} \text{Im} \left[\frac{m^2}{m^2 - 1} \ln(m^2) \right], \quad (15)$$

where $k = 2\pi/\lambda$ is the wavenumber, $V = \frac{4}{3}\pi r_{\text{ve}}^3$ is the volume of particles, and $\ln(z)$ denotes the principle logarithm of z . The extinction cross section can then be calculated according to Eq. (12). The CDE model has previously been applied to model the infrared absorption features of quartz particles [32,51], and is commonly used within astronomy literature to model the extinction spectra of silicate as well as non-silicate cosmic dust particles [73–75].

The T -matrix method is an exact technique for numerically solving Maxwell's equations to determine the light scattering of non-spherical particles [76,77]. The approach of modelling extinction using a distribution of spheroidal shapes, computed using T -matrix theory, has widely been applied to atmospheric dust

[38,43,78] and its individual components including quartz [44,79]. In this work, the *T*-matrix code available from NASA (https://www.giss.nasa.gov/staff/mmishchenko/t_matrix.html) and detailed in [80] has been used. The *T*-matrix code allows the cross section per particle to be calculated for a lognormal distribution of particle sizes (specified in terms of their volume equivalent radius) in which all particles have the same spheroidal shape. The spheroidal shape is defined in terms of the axial ratio, $\epsilon = a/b$, where a is the major axis of the spheroid and b is the minor axis. It is convenient to define the shape factor, ξ , of spheroids as:

$$\xi = \begin{cases} \epsilon - 1, & \text{for } \epsilon \geq 1 \text{ (oblate)} \\ 1 - (1/\epsilon), & \text{for } \epsilon < 1 \text{ (prolate)} \end{cases} \quad (16)$$

For each sample, the lognormal fits to the measured size distribution and literature complex refractive index values were inputs to the *T*-matrix code and were used to generate average extinction cross sections per particle, $\langle \sigma^{\text{ext}}(\xi, \lambda) \rangle$, for spheroidal shape factors in the range $-4 \leq \xi \leq 9$ at intervals of $\Delta\xi = 0.5$. For all samples, the lognormal distributions provided good fits to the measured size distributions. The calculations were restricted to wavelengths in the range $7.5 \leq \lambda \leq 13.5 \mu\text{m}$, and the resolution of the calculations was 200 points evenly spaced by wavelength. It was found that applying the code to shorter wavelengths or more extreme spheroidal shape factors resulted in computations which failed to converge. Once the spheroidal cross sections were calculated for the set of shape factors, the cumulative extinction per particle, $\langle \sigma_{\text{tot}}^{\text{ext}} \rangle$, of the system could be modelled as a weighted average:

$$\langle \sigma_{\text{tot}}^{\text{ext}} \rangle = \sum_i w_i \langle \sigma^{\text{ext}}(\xi_i) \rangle, \quad (17)$$

subject to,

$$\sum_i w_i = 1. \quad (18)$$

where w_i are the individual weightings. The values of w_i were retrieved using the Levenberg–Marquardt method to determine the best fit to the experimental data. In this way the distribution of spheroidal shapes that best fitted the experimental data was identified.

4.2. Literature complex refractive indices and birefringence of crystalline quartz

Literature values for the complex refractive index of crystalline and amorphous silica were assumed in order to model the spectral extinction. Crystalline α -quartz has uniaxial birefringence and its complex refractive index is described by the ordinary, m_o (parallel to the optical axis), and the extraordinary component, m_e (perpendicular to the optical axis). Two methods were investigated for averaging the ordinary and extraordinary components to model the extinction cross section. The optical constants averaging (OCA) method involved using the weighted average complex refractive index, $m = \frac{2}{3}m_o + \frac{1}{3}m_e$, to compute extinction cross sections. The spectral averaging (SA) method involved individually computing cross sections for m_o and m_e and then calculating the weighted average extinction cross section according to: $\sigma^{\text{ext}} = \frac{2}{3}\sigma_o^{\text{ext}} + \frac{1}{3}\sigma_e^{\text{ext}}$.

The tabulated band parameters for the birefringent complex refractive index of crystalline quartz, determined by [81], were used for wavelengths in the range 3.0–19 μm . For wavelengths in the range 0.33–3.0 μm , the dispersion formula for the real refractive index of crystalline quartz found by [64] was used and the imaginary refractive index was taken to be zero.

For amorphous silica, the complex refractive index measured by [82] in the range 1.54–14.3 μm was used, and in the range 0.33–1.25 μm values measured by [65] were used. The real and imagi-

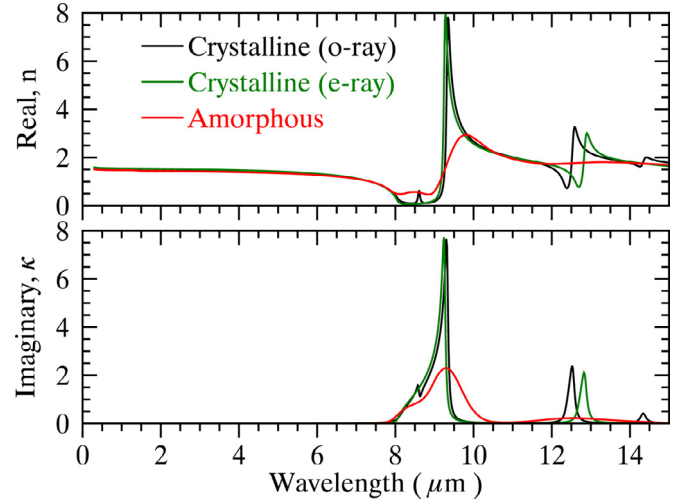


Fig. 7. The complex refractive index of crystalline and amorphous silicon dioxide.

Table 3

R^2 values for the various scattering models against the experimental data.

Model	Sample A (crystalline)	Sample B (crystalline)	Sample C (amorphous)
Mie (7.5–13.5 μm)	0.19 (SA) 0.17 (OCA)	0.18 (SA) 0.16 (OCA)	0.86
Mie (0.33–7.5 μm)	0.97 (SA) 0.97 (OCA)	0.92 (SA) 0.92 (OCA)	0.98
CDE (7.5–13.5 μm)	0.96 (SA) 0.96 (OCA)	0.82 (SA) 0.82 (OCA)	0.98
CDE (0.33–7.5 μm)	0.55 (SA) 0.55 (OCA)	0.26 (SA) 0.26 (OCA)	0.52
<i>T</i> -matrix (7.5–13.5 μm)	0.91 (SA) 0.91 (OCA)	0.74 (SA) 0.72 (OCA)	0.995
<i>T</i> -matrix (mixture)	0.98 (SA) 0.98 (OCA)	0.97 (SA) 0.97 (OCA)	–

nary refractive index in the region (1.25–1.54 μm) were estimated by linear interpolation.

Fig. 7 shows the assumed complex refractive indices of crystalline and amorphous silicon dioxide. For crystalline silica, both the ordinary and extraordinary components are shown. The infrared features, associated with Si–O–Si vibrations, of crystalline silica have much higher and narrower peaks than those of amorphous silica. There are small wavelength shifts between the features of the ordinary and extraordinary rays.

4.3. Modelling results and discussion

4.3.1. Mie theory and the CDE model

Fig. 8 shows measured versus modelled extinction calculated with Mie theory and the CDE model. The calculations required the measured in-cell size distributions and the literature complex refractive indices as inputs. The in-cell size distributions were calculated as detailed in Section 3.3, and no additional scaling was performed. The left column shows the full spectral range with a logarithmic wavelength scale, whereas the right column shows the infrared absorption features. Each row shows a different sample.

For the two crystalline samples, Mie theory poorly represents the 9 μm absorption feature; the measured peak height is much smaller and the measured peak width is greater than that predicted by assuming spherical scatterers. The CDE model provides an improved fit to the experimental data in the infrared. Values of the coefficient of determination (R^2) for the model fits to the data are detailed in Table 3. Sample A, for example, at wavelengths

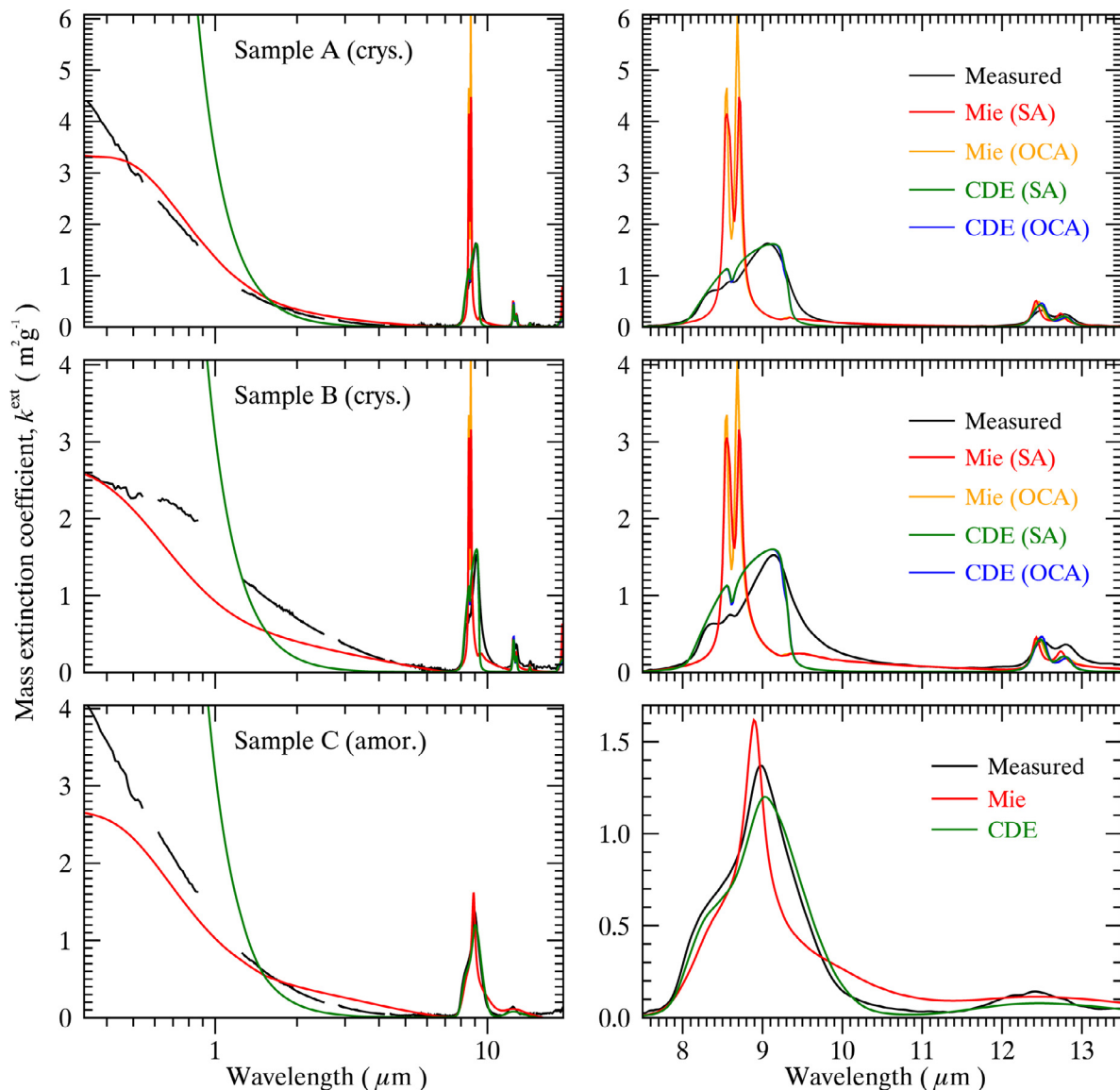


Fig. 8. Modelled extinction using Mie theory and the CDE. For the birefringent crystalline samples two methods of averaging the o-ray and e-ray components were used: the spectral averaging (SA) method and the optical constants averaging (OCA) method.

7.5–13.5 μm has R^2 values for Mie theory against the experimental data of 0.19 and 0.17 for the spectral averaging and optical constant averaging methods. This is compared to a value of 0.96 for both averaging methods and the CDE model. However, the CDE model provides a significantly better fit to Sample A compared to Sample B; this is largely due to the broader 9 μm feature of Sample B (particularly for $\lambda > 9.4 \mu\text{m}$) which is not well represented by the CDE and the assumed refractive index. The CDE model is valid in the Rayleigh approximation; based on a mean particle radius of 0.13 μm , the size parameter is 0.11–0.06 (for wavelengths 7.5–13.5 μm), and therefore the approximation can be considered reasonable.

For amorphous silica (Sample C), the differences between Mie theory and the CDE model for the infrared absorption features are significantly less, although the CDE model still performs better indicating the particles have a significant degree of non-sphericity. The R^2 values for Mie theory and the CDE model are 0.86 and 0.98 (across wavelengths 7.5–13.5 μm), respectively. The fact that the CDE model (representing an extreme distribution of particle shapes) is much closer to Mie theory for the amorphous sample

compared to the crystalline samples shows that non-spherical effects are much more significant when there are extreme features in the complex refractive index (the peaks in refractive index shown in Fig. 7 are much higher for crystalline quartz).

At shorter wavelengths (0.33–7.5 μm), Mie theory matches the experimental extinction with varying success: R^2 values are 0.97, 0.92 and 0.98 for samples A, B and C, respectively. Although the R^2 values are fairly high, the plots show significant deviations between the theory and the experimental data. For example, Sample B shows differences as large as 100 % at around 0.8 μm . These differences may be the results of non-spherical scattering effects, uncertainty in the size distribution, or uncertainty in the assumed complex refractive index. The showtwave extinction is dominated by scattering and is particularly sensitive to the large particle tail of the size distribution measured by the OPC. The OPC uses Mie theory, inverting the measured scattered intensity to determine particle size. Non-spherical scattering effects will therefore introduce systematic error into the size distribution returned by the OPC. The validity of the Rayleigh approximation breaks down at

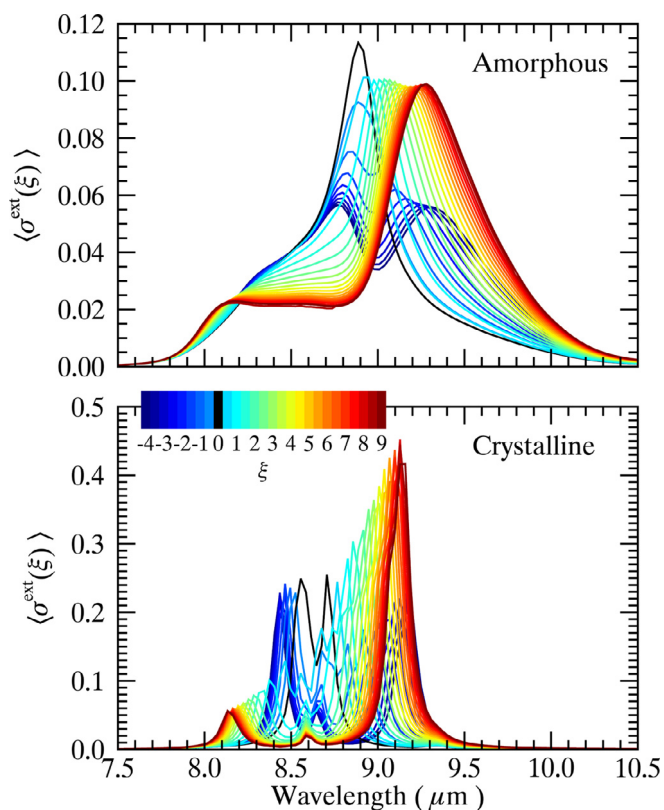


Fig. 9. Spheroidal cross sections per particle, $\langle \sigma^{\text{ext}}(\xi) \rangle$, computed using *T*-matrix theory, as a function of the shape parameter, ξ . The plot shows the Si–O–Si asymmetric vibration feature only, although the *T*-matrix calculations were performed across the wider wavelength range of 7.5–13.5 μm .

shorter wavelength and the CDE model predicts unrealistically high MEC values; values of R^2 are low.

4.3.2. *T*-matrix modelling of a distribution of spheroids

Fig. 9 shows how the spheroidal cross sections per particle, $\langle \sigma^{\text{ext}}(\xi) \rangle$, calculated using *T*-matrix theory, vary with the shape factor, ξ . The top plot shows the results assuming the amorphous complex refractive index and the measured size distribution of Sample C (amorphous) whereas the lower plot shows results assuming the crystalline complex refractive index and the size distribution of Sample A (crystalline); differences between $\langle \sigma^{\text{ext}}(\xi) \rangle$ for the two crystalline samples were small. Differences between the *T*-matrix results for spheres ($\xi = 0$) and the Mie theory results were negligible, as expected.

Fig. 9 demonstrates that the cross sections vary significantly when the crystalline or the amorphous complex refractive index is assumed. The peaks are much narrower and higher in the crystalline case compared to those for the amorphous sample (note the different scale on the y-axis between the upper and lower plots); although both cases show the expected pattern of the feature broadening as the shape factor deviates from zero (spheres) to more oblate ($\xi \geq 1$) or prolate ($\xi < 1$) shape factors. The broadening is much more significant for the amorphous case; the relative extinction at $\lambda > 9.3 \mu\text{m}$ compared to the peak extinction is greater, particularly for highly non-spherical particles.

Fig. 10 shows fits to the experimental data using the *T*-matrix spheroidal cross sections. The relative weightings, w_i , of the cross sections were retrieved – according to Eqs. (17) and (18) – to give the best fit to the experimental data. In Fig. 10, model fits to the experimental data are shown by the plots on the left, whilst the retrieved relative weightings are shown by the bar-plots to the right.

For the two crystalline sample, two retrievals were performed: one using cross sections generated using the crystalline complex refractive index only; and a second using both amorphous and crystalline cross sections (assuming an external mixture of crystalline and amorphous particles, both having the same particle size distribution).

Considering the amorphous result first (Sample C), Fig. 10 shows that the *T*-matrix approach provides an excellent fit to the experimental data; the R^2 value for the fit is 0.995. The fit to the 9 μm absorption feature is very good, but the modelled extinction slightly underestimates the extinction of the 12.5 μm feature. For the crystalline samples (Sample A and Sample B), the quality of the fit using only crystalline cross sections is noticeably better for Sample A (R^2 of 0.91 for the SA method) compared to Sample B (R^2 of 0.72 for the SA method). However, in both cases the measured extinction feature at 9 μm is broader than the modelled version. The retrieved weightings, w_i , for the two samples are similar showing a central grouping clustered around $\xi = 2$, and relatively high weightings for the extreme prolate ($\xi = 9$) and the extreme oblate ($\xi = -4$) cross sections. This may reflect the presence of highly non-spherical particles within the quartz samples.

When Sample A and Sample B are modelled as an external mixture containing both crystalline and amorphous spheroids, the quality of the fits significantly improves particularly with respect to the model's ability to represent the width of the 9 μm feature. R^2 values for the mixture approach are significantly higher at 0.98 for Sample A and 0.97 for Sample B. The retrieved weightings suggest that Sample A has an amorphous content of 29 % and Sample B contains 56 %, by mass. For the mixture retrieval, the crystalline component of the weightings shows a similar distribution to the crystalline only retrievals, whereas the amorphous component has only a single weighting with a non-zero value.

The improved fits modelling Sample A and Sample B as a mixture of amorphous and crystalline particles may indicate that a significant number of particles have reduced crystallinity. The model approach of treating particles as either purely crystalline or purely amorphous may not necessarily be true; one might expect particles to have varying degrees of crystallinity or there may be a uniform distribution whereby particles have similar polycrystalline structures that lie somewhere between purely crystalline or purely amorphous. The crystallinity of powdered quartz samples is known to affect optical properties including infrared absorption features, and has been shown to vary with differences in the production process in particular the milling time [70,71].

5. Conclusions

This paper details an experimental apparatus capable of accurately measuring the spectral mass extinction, at 0.33–19 μm , and size distribution of solid aerosol particles dispersed in nitrogen gas. Initial measurements on high purity crystalline and amorphous silica samples have been presented. The experimental data have been compared to the extinction predicted by three scattering models: Mie theory, the Rayleigh CDE model, and *T*-matrix theory applying a distribution of spheroids. In each case using literature values for the complex refractive index and the measured size distribution as model inputs.

The apparatus used the WDF (manufactured by EMMS) to disperse the powdered samples into the aerosol cell. The WDF was effective in providing a reproducible and near-constant number density of dispersed aerosol into the gas flow, allowing repeated spectral and sizing measurements of the aerosol and good estimates of measurement uncertainty. Mass loading filter measurements provided a high level of confidence in the mass of aerosol per unit

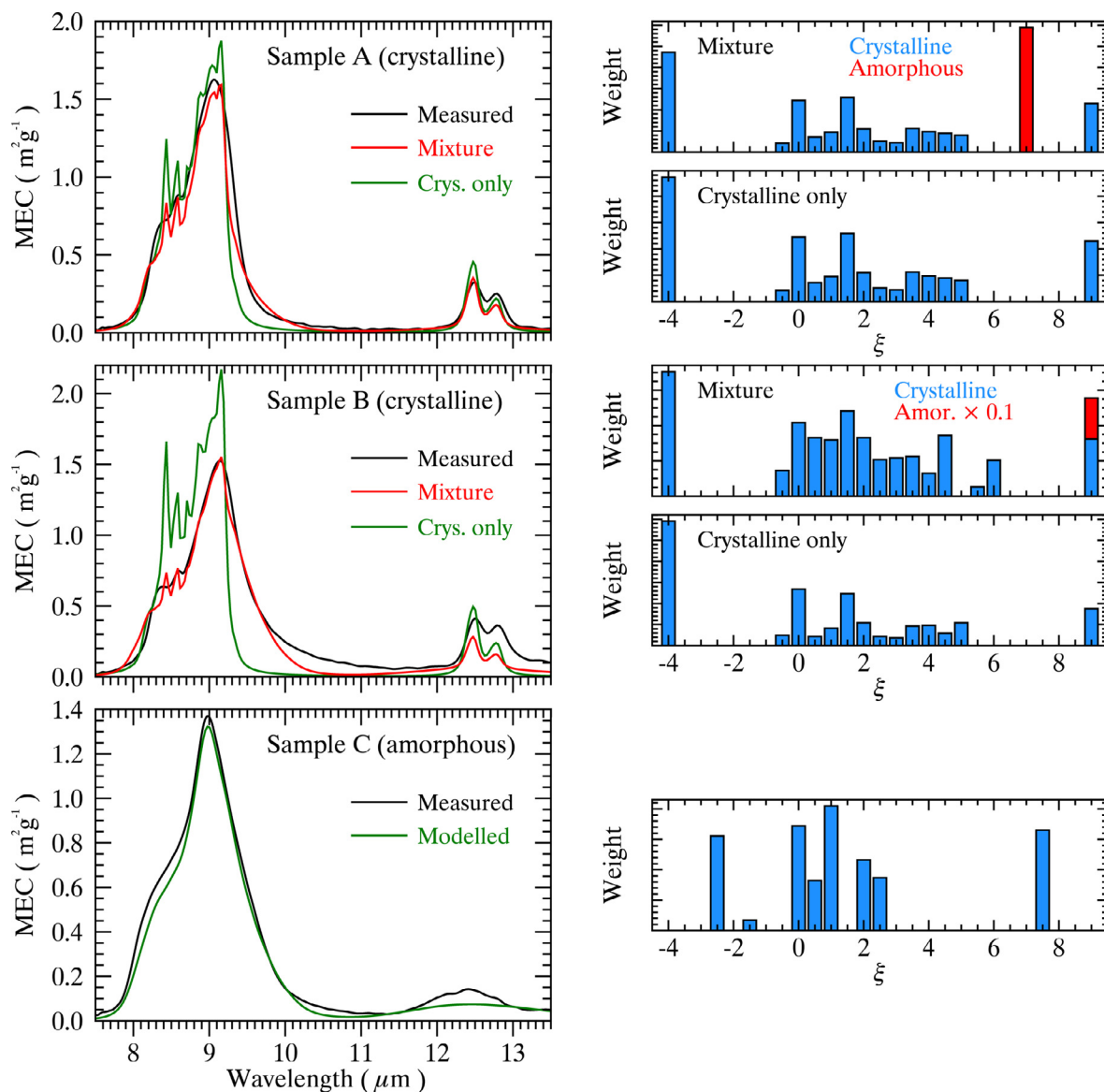


Fig. 10. T-matrix retrieval results. Cross sections generated using different shape parameters, $(\sigma^{\text{ext}}(\xi, \lambda))$, were used to fit the measured spectral extinction. The plots on the left show the fits to the data and the bar-plots on the right show the retrieved weightings of the cross sections. The weightings sum to 1. For the crystalline samples fits were also performed allowing a mixture of crystalline and amorphous cross sections.

volume inside the cell, allowing the dilution between the cell and sizing instruments to be accurately calibrated.

Relative humidity is known to affect aerosol scattering properties [66]. It is therefore important to quote the relative humidity at which spectral extinction measurements are performed. The in-cell relative humidity during experiments was determined from gas concentrations retrievals applying the RFM [59]. The gas lines were removed from the spectral extinction, leaving the aerosol component only.

The modelling results confirm that Mie theory provides a poor fit to the infrared extinction features of quartz. However, the discrepancies between amorphous silica and Mie theory are significantly lower. This is due to differences in the complex refractive index: the infrared features of the complex refractive index of crystalline quartz show significantly narrower and higher peaks compared to the more smoothly varying features of amorphous silica. The differences between the infrared extinction predicted by the Rayleigh CDE model and Mie theory when the amorphous refractive index is assumed are relatively small compared to the large

differences in the model predictions for crystalline quartz. This emphasises that non-spherical scattering effects are more significant close to strong refractive index features. The significant effect of non-sphericity in cases of extreme refractive index features is further reiterated by the differences in the T-matrix spheroidal cross sections with varying aspect ratio when the crystalline refractive index of quartz (extreme refractive index features) is used as an input compared to when the complex refractive index of amorphous quartz is assumed. The cross sections vary much more significantly as a function of aspect ratio for quartz compared to amorphous silica.

The modelling results show that the Rayleigh CDE model provides remarkably good fits (given the simplicity of the analytic expressions) to the infrared extinction data of both crystalline and amorphous silica. At shorter wavelengths, the validity of the Rayleigh approximation breaks down and the fit to the experimental data rapidly deteriorates. However, the CDE model has been shown to provide poor fits to the infrared extinction features of other important components of mineral dust such as cal-

cite and dolomite (even within the Rayleigh regime) [51]. The significant advantage of T -matrix methods, assuming a distribution of spheroids, is their versatility in matching light scattering properties of many atmospheric aerosols of different shapes [44,45].

T -matrix methods were used to model the measured infrared extinction of silica: cross sections were calculated for a wide distribution of spheroidal shape factors and retrievals was performed to find the weightings of cross sections (constraining the total number of particles according to the measured size distributions) that best fitted the experimental data. The fit to the experimental data for amorphous quartz was excellent. For the two crystalline samples it was found that combining amorphous and crystalline cross sections provided a significantly improved fit to the data compared to using crystalline cross sections only. The fits using the mixture approach were very good, with R^2 values above 0.97. This indicates that the crystallinity of the quartz samples may have been reduced by the milling process. This is consistent with previous investigations of the crystallinity of milled quartz powders [70,71].

The T -matrix calculations could only be applied to infrared wavelengths; at shorter wavelengths the code failed to converge. However, Mie theory provided reasonably good fits to the modelled extinction for wavelengths in the range 0.33–7.5 μm . R^2 values were above 0.92 for all samples in this wavelength range.

The quality of the T -matrix fits to the experimental data supports the accuracy of the extinction and sizing measurements. The fits using the T -matrix approach and the CDE model are consistent with previous investigations of silica particles [32,44,51]. The work presented here provides some improvements over previous studies. An experimental method has been developed which is capable of measuring the particle size distribution and spectral extinction over the complete range of wavelengths relevant to atmospheric radiative transfer at a higher spectral resolution than previous measurements of quartz. Furthermore, we provide estimates of the measurement uncertainty associated with the mass extinction coefficients. In the future, results for the mass extinction coefficient and size distribution of various volcanic ash samples, as well as candidate geo-engineering particles, will be presented.

Acknowledgements

R.G.G. and D.M.P. acknowledge funding from the NERC VANAHEIM project NE/1015592/1 and the NERC SHIVA project NE/J023310/1. B.E.R. was funded by a NERC studentship NE/J500045/1. This study was funded as part of NERCs support of the National Centre for Earth Observation and the Centre for Observation and Modelling of Earthquakes, Volcanoes, and Tectonics.

References

- [1] Satheesh S, Moorthy KK. Radiative effects of natural aerosols: a review. *Atmosph Env* 2005;39(11):2089–110. <http://www.sciencedirect.com/science/article/pii/S135223100500018X> doi: 10.1016/j.atmosenv.2004.12.029.
- [2] Osborne SR, Baran AJ, Johnson BT, Haywood JM, Hesse E, Newman S. Short-wave and long-wave radiative properties of saharan dust aerosol. *Q J R Meteorol Soc* 2011;137(658):1149–67. doi:10.1002/qj.771.
- [3] Rosenfeld D, Lohmann U, Raga GB, O'Dowd CD, Kulmala M, Fuzzi S, et al. Flood or drought: how do aerosols affect precipitation? *Science* 2008;321(5894):1309–13. <http://science.sciencemag.org/content/321/5894/1309.full.pdf> doi: 10.1126/science.1160606.
- [4] Nickovic S, Cvetkovic B, Madonna F, Rosoldi M, Pejanovic G, Petkovic S, et al. Cloud ice caused by atmospheric mineral dust—part 1: parameterization of ice nuclei concentration in the NMME-DREAM model. *Atmosph Chem Phys* 2016;16(17):11367–78. <http://www.atmos-chem-phys.net/16/11367/2016/> doi: 10.5194/acp-16-11367-2016.
- [5] George IJ, Abbatt JPD. Heterogeneous oxidation of atmospheric aerosol particles by gas-phase radicals. *Nat Chem* 2010;2(9):713–22. doi:10.1038/nchem.806.
- [6] Boucher O, Randall D, Artaxo P, Bretherton C, Feingold G, Forster P, et al. Clouds and aerosols. In: Stocker T, Qin D, Plattner G-K, Tignor M, Allen S, Boschung J, et al., editors. *Climate change 2013: the physical science basis*. Contribution of working group I to the fifth assessment report of the intergovernmental panel on climate change; book section. Cambridge, United Kingdom and New York, NY, USA: Cambridge University Press; 2013. p. 571–658. www.climatechange2013.org, doi: 10.1017/CBO9781107415324.016 ISBN 978-1-107-66182-0.
- [7] Christopher SA, Johnson B, Jones TA, Haywood J. Vertical and spatial distribution of dust from aircraft and satellite measurements during the GERBILLS field campaign. *Geophys Res Lett* 2009;36(6). L06806 doi: 10.1029/2008GL037033.
- [8] Ginoux P, Prospero JM, Gill TE, Hsu NC, Zhao M. Global-scale attribution of anthropogenic and natural dust sources and their emission rates based on MODIS deep blue aerosol products. *Rev Geophys* 2012;50(3). RG3005 doi: 10.1029/2012RG000388.
- [9] Denjean C, Cassola F, Mazzino A, Triquet S, Chevaillier S, Grand N, et al. Size distribution and optical properties of mineral dust aerosols transported in the western mediterranean. *Atmosph Chem Phys* 2016;16(2):1081–104. <http://www.atmos-chem-phys.net/16/1081/2016/> doi: 10.5194/acp-16-1081-2016.
- [10] Choobari OA, Zavar-Reza P, Sturman A. The global distribution of mineral dust and its impacts on the climate system: a review. *Atmosph Res* 2014;138:152–65. <http://www.sciencedirect.com/science/article/pii/S0169809513003281> doi: 10.1016/j.atmosres.2013.11.007.
- [11] Athanasopoulou E, Protonotariou A, Papangelis G, Tombrou M, Mihalopoulos N, Gerasopoulos E. Long-range transport of saharan dust and chemical transformations over the eastern mediterranean. *Atmosph Env* 2016;140:592–604. <http://www.sciencedirect.com/science/article/pii/S1352231016304745> doi: 10.1016/j.atmosenv.2016.06.041.
- [12] Ganor E. The frequency of saharan dust episodes over tel aviv, israel. *Atmosph Env* 1994;28(17):2867–71. <http://www.sciencedirect.com/science/article/pii/S1352231094900876> doi: 10.1016/1352-2310(94)90087-6.
- [13] Yin D, Nickovic S, Barbaris B, Chandby B, Sprigg WA. Modeling wind-blown desert dust in the southwestern united states for public health warning: a case study. *Atmosph Env* 2005;39(33):6243–54. <http://www.sciencedirect.com/science/article/pii/S1352231005005947> doi: 10.1016/j.atmosenv.2005.07.009.
- [14] Ansmann A, Bösenberg J, Chaikovskiy A, Comerón A, Eckhardt S, Eixmann R, et al. Long-range transport of saharan dust to northern europe: the 11–16 october 2001 outbreak observed with EARLINET. *J Geophys Res* 2003;108(D24). 4783 doi: 10.1029/2003JD003757.
- [15] Swap R, Garstang M, Greco S, Talbot R, Källberg P. Saharan dust in the amazon basin. *Tellus B* 2011;44(2). <http://www.tellusb.net/index.php/tellusb/article/view/15434>
- [16] Gibbs G, Heaney P, Prewitt C. *Silica: physical behavior, geochemistry and materials applications*, 29. Mineralogical Society of America; 1994.
- [17] Thomas M, Gautier C. Investigations of the march 2006 african dust storm using ground-based column-integrated high spectral resolution infrared (8–13 μm) and visible aerosol optical thickness measurements: 2. mineral aerosol mixture analyses. *J Geophys Res* 2009;114(D14). D14209 doi: 10.1029/2008JD010931.
- [18] Sokolik IN, Toon OB. Incorporation of mineralogical composition into models of the radiative properties of mineral aerosol from UV to IR wavelengths. *J Geophys Res* 1999;104(D8):9423–44. doi:10.1029/1998JD200048.
- [19] Cashman K, Rust A. Introduction. In: Mackie S, Cashman K, Ricketts H, Rust A, Watson M, editors. *Volcanic ash*. Elsevier; 2016. p. 5–22. ISBN 978-0-08-100405-0. <http://www.sciencedirect.com/science/article/pii/B9780081004050000021> doi: 10.1016/B978-0-08-100405-0.00002-1.
- [20] Reed BE. Measurements of the complex refractive index of volcanic ash. University of Oxford; 2017. Ph.D. thesis. <http://eodg.atm.ox.ac.uk/eodg/theses/Reed.pdf>
- [21] Dunn MG, Wade DP. Influence of volcanic ash clouds on gas turbine engines. In: Casadevall TJ, editor. *Proceedings of the first international symposium on volcanic ash and aviation safety*. USGS Bulletin 2047; 1994. p. 107–17. Washington
- [22] Przedpelski ZJ, Casadevall TJ. Impact of volcanic ash from 15 December 1989 Redoubt volcano eruption on GE CF6–80C2 Turbofan engines. In: Casadevall TJ, editor. *Proceedings of the first international symposium on volcanic ash and aviation safety*. U.S. Geological Survey Bulletin B 2047; 1994. p. 129–35.
- [23] Guffanti M, Casadevall TJ, Budding K. Encounters of aircraft with volcanic ash clouds; A compilation of known incidents, 1953–2009. Tech. Rep. U.S. Geological Survey; 2010. <http://pubs.usgs.gov/ds/545>.
- [24] Gudmundsson MT, Thordarson T, Höskuldsson A, Larsen G, Björnsson H, Prata FJ, et al. Ash generation and distribution from the april–may 2010 eruption of eyjafjallajökull, iceland. *Sci Rep* 2012;2(572). doi:10.1038/srep00572.
- [25] Oxford Economics. *The economic impacts of air travel restrictions due to volcanic ash*, report. Oxford, UK: Abbey House; 2010.
- [26] European Union. *Volcano crisis report: Report on the actions undertaken in the context of the impact of the volcanic ash cloud crisis on the air transport industry*. Brussels: Eur. Comm.; 2010.
- [27] Wang Y, Sakamaki T, Skinner LB, Jing Z, Yu T, Kono Y, et al. Atomistic insight into viscosity and density of silicate melts under pressure. *Nat Commun* 2014;5. doi:10.1038/ncomms4241.
- [28] Di Genova D, Morgavi D, Hess K-U, Neuville DR, Borovkov N, Perugini D, et al. Approximate chemical analysis of volcanic glasses using raman spectroscopy. *J Raman Spectrosc* 2015;46(12):1235–44. JRS-15-0075.R3 doi: 10.1002/jrs.4751.
- [29] Grainger RG, Peters DM, Thomas GE, Smith AJA, Siddans R, Carboni E, et al. Measuring volcanic plume and ash properties from space. In: Pyle DM, Mather TA, Biggs J, editors. *Remote sensing of volcanoes and volcanic processes: integrating observation and modelling*, 380. Geol. Soc. London Spec. Publ.; 2013. p. 293–320. doi:10.1144/SP380.7.

- [30] Prata AJ, Dezitter F, Davies I, Weber K, Birnfeld M, Moriano D, et al. Artificial cloud test confirms volcanic ash detection using infrared spectral imaging. *Sci Rep* 2016;6. doi:10.1038/srep25620.
- [31] Prata AJ. Observations of volcanic ash clouds in the 10–12 μm window using AVHRR/2 data. *Int J Remote Sens* 1989;10:751–61.
- [32] Bohren CF, Huffman DR. *Absorption and scattering of light by small particles*. John Wiley & Sons; 1983.
- [33] Moorthy KK, Satheesh SK, Babu SS, Dutt CBS. Integrated campaign for aerosols, gases and radiation budget (ICARB): an overview. *J Earth Syst Sci* 2008;117(1):243–62. doi:10.1007/s12040-008-0029-7.
- [34] Su W, Loeb NG, Schuster GL, Chin M, Rose FG. Global all-sky shortwave direct radiative forcing of anthropogenic aerosols from combined satellite observations and GOCART simulations. *J Geophys Res* 2013;118(2):655–69. doi:10.1029/2012JD018294.
- [35] Myhre G, Samset BH, Schulz M, Balkanski Y, Bauer S, Bernsten TK, et al. Radiative forcing of the direct aerosol effect from aerocom phase II simulations. *Atmosph Chem Phys* 2013;13(4):1853–77. <http://www.atmos-chem-phys.net/13/1853/2013/> doi: 10.5194/acp-13-1853-2013.
- [36] Huffman DR, Bohren CF. Infrared absorption spectra of non-spherical particles treated in the Rayleigh-ellipsoid approximation. In: Schuerman DW, editor. *Light scattering by irregularly shaped particles*; chap. 4. Boston, MA: Springer US; 1980. p. 103–11. ISBN 978-1-4684-3704-1. doi:10.1007/978-1-4684-3704-1_13.
- [37] Haapanala P, Räisänen P, Kahnert M, Nousiainen T. Sensitivity of the short-wave radiative effect of dust on particle shape: comparison of spheres and spheroids. *J Geophys Res* 2012;117(D8). D08201 doi: 10.1029/2011JD017216
- [38] Alexander JM, Laskina O, Meland B, Young MA, Grassian VH, Kleiber PD. A combined laboratory and modeling study of the infrared extinction and visible light scattering properties of mineral dust aerosol. *J Geophys Res* 2013;118(2):435–52. doi:10.1029/2012JD018751.
- [39] Nousiainen T, Zubko E, Niemi JV, Kupiainen K, Lehtinen M, Muinonen K, et al. Single-scattering modeling of thin, birefringent mineral-dust flakes using the discrete-dipole approximation. *J Geophys Res* 2009;114(D7). D07207 doi: 10.1029/2008JD011564.
- [40] Lindqvist H, Nousiainen T, Zubko E, Munõz O. Optical modeling of vesicular volcanic ash particles. *J Quant Spectrosc Radiat Transf* 2011;112(11):1871–80. <http://www.sciencedirect.com/science/article/pii/S0022407311000574> doi: 10.1016/j.jqsrt.2011.01.032.
- [41] Yang P, Liou KN, Mishchenko MI, Gao B-C. Efficient finite-difference time-domain scheme for light scattering by dielectric particles: application to aerosols. *Appl Opt* 2000;39(21):3727–37. <http://ao.osa.org/abstract.cfm?URI=ao-39-21-3727> doi: 10.1364/AO.39.003727.
- [42] Ishimoto H, Masuda K, Fukui K, Shimbori T, Inazawa T, Tuchiya H, et al. Estimation of the refractive index of volcanic ash from satellite infrared sounder data. *Remote Sens Env* 2016;174:165–80. <http://www.sciencedirect.com/science/article/pii/S0034425715302303> doi: 10.1016/j.rse.2015.12.009.
- [43] Mishchenko MI, Travis LD, Kahn RA, West RA. Modeling phase functions for dustlike tropospheric aerosols using a shape mixture of randomly oriented polydisperse spheroids. *J Geophys Res* 1997;102(D14):16831–47. doi:10.1029/96JD02110.
- [44] Kleiber PD, Grassian VH, Young MA, Hudson PK. T-Matrix studies of aerosol particle shape effects on ir resonance spectral line profiles and comparison with an experiment. *J Geophys Res* 2009;114(D21). D21209 doi: 10.1029/2009JD012710.
- [45] Nousiainen T, Kahnert M, Veihelmann B. Light scattering modeling of small feldspar aerosol particles using polyhedral prisms and spheroids. *J Quant Spectrosc Radiat Transf* 2006;101(3):471–87. *Light in Planetary Atmospheres and Other Particulate Media*; <http://www.sciencedirect.com/science/article/pii/S0022407306000483> doi: 10.1016/j.jqsrt.2006.02.038.
- [46] Mishchenko MI, Videen G, Babenko VA, Khlebtsov NG, Wriedt T. T-Matrix theory of electromagnetic scattering by particles and its applications: a comprehensive reference database. *J Quant Spectrosc Radiat Transf* 2004;88(1):357–406. <http://www.sciencedirect.com/science/article/pii/S0022407304001372> doi: 10.1016/j.jqsrt.2004.05.002.
- [47] Dubovik O, Sinyuk A, Lapyonok T, Holben BN, Mishchenko M, Yang P, et al. Application of spheroid models to account for aerosol particle nonsphericity in remote sensing of desert dust. *J Geophys Res* 2006;111(D11). doi:10.1029/2005JD006619. D11208
- [48] Veselovskii I, Dubovik O, Kolgotin A, Lapyonok T, Di Girolamo P, Summa D, et al. Application of randomly oriented spheroids for retrieval of dust particle parameters from multiwavelength lidar measurements. *J Geophys Res* 2010;115(D21). doi:10.1029/2010JD014139. D21203
- [49] Hudson PK, Gibson ER, Young MA, Kleiber PD, Grassian VH. A newly designed and constructed instrument for coupled infrared extinction and size distribution measurements of aerosols. *Aerosol Sci Technol* 2007;41(7):701–10. doi:10.1080/02786820701408509.
- [50] Hudson PK, Gibson ER, Young MA, Kleiber PD, Grassian VH. Coupled infrared extinction and size distribution measurements for several clay components of mineral dust aerosol. *J Geophys Res* 2008a;113(D1). D01201 doi: 10.1029/2007JD008791.
- [51] Hudson PK, Young MA, Kleiber PD, Grassian VH. Coupled infrared extinction spectra and size distribution measurements for several non-clay components of mineral dust aerosol (quartz, calcite, and dolomite). *Atmosph Env* 2008b;42(24):5991–9. <http://www.sciencedirect.com/science/article/pii/S1352231008003154> doi: 10.1016/j.atmosenv.2008.03.046.
- [52] Mogili PK, Yang KH, Young MA, Kleiber PD, Grassian VH. Environmental aerosol chamber studies of extinction spectra of mineral dust aerosol components: broadband ir-uv extinction spectra. *J Geophys Res* 2007;112(D21). n/a-n/a D21204 doi: 10.1029/2007JD008890.
- [53] Smith AJA, Peters DM, McPheat R, Lukanihins S, Grainger RG. Measuring black carbon spectral extinction in the visible and infrared. *J Geophys Res* 2015;120(18):9670–83. 2015JD023564 doi: 10.1002/2015JD023564.
- [54] McPheat RA, Newnham DA, Williams RG, Ballard J. Large-volume, coolable spectroscopic cell for aerosol studies. *Appl Opt* 2001;40(36):6581–6. <http://ao.osa.org/abstract.cfm?URI=ao-40-36-6581> doi: 10.1364/AO.40.006581.
- [55] von der Weiden S-L, Drewnick F, Borrmann S. Particle loss calculator – a new software tool for the assessment of the performance of aerosol inlet systems. *Atmosph Measure Tech* 2009;2(2):479–94. <http://www.atmos-meas-tech.net/2/479/2009/> doi: 10.5194/amt-2-479-2009.
- [56] White JU. Long optical paths of large aperture. *J Opt Soc Am* 1942;32:285–8. doi:10.1364/JOSA.32.000285.
- [57] Bence JR. Analysis of short time series: correcting for autocorrelation. *Ecology* 1995;76(2):628–39. doi:10.2307/1941218.
- [58] Working Group 1. Evaluation of measurement data – Guide to the expression of uncertainty in measurement. *Tech. Rep.*, JCGM 100:2008. Joint Committee for Guides in Metrology; 2008. <http://www.iso.org/sites/JCGM/GUM-introduction.htm>
- [59] Dudhia A. The reference forward model (RFM). *J Quant Spectrosc Radiat Transf* 2017;186:243–53. *Satellite Remote Sensing and Spectroscopy: Joint ACE-Odin Meeting, October 2015*; <http://www.sciencedirect.com/science/article/pii/S0022407316301029> doi: 10.1016/j.jqsrt.2016.06.018.
- [60] Rodgers CD. *Inverse methods for atmospheric sounding: theory and practice*. World Scientific; 2000.
- [61] Buck AL. New equations for computing vapor pressure and enhancement factor. *J Appl Meteorol* 1981;20(12):1527–32. doi:10.1175/1520-0450.
- [62] DeCarlo PF, Slowik JG, Worsnop DR, Davidovits P, Jimenez JL. Particle morphology and density characterization by combined mobility and aerodynamic diameter measurements. part 1: theory. *Aerosol Sci Technol* 2004;38:1185–205. doi:10.1080/027868290903907.
- [63] Allen MD, Raabe OG. Slip correction measurements of spherical solid aerosol particles in an improved millikan apparatus. *Aerosol Sci Technol* 1985;4(3):269–86. doi:10.1080/02786828508959055.
- [64] Radhakrishnan T. Further studies on the temperature variation of the refractive index of crystals. *Proc Ind Acad Sci Section A* 1951;33(1):22. doi:10.1007/BF03172255.
- [65] Gao L, Lemarchand F, Lequime M. Refractive index determination of SiO_2 layer in the UV/vis/NIR range: spectrophotometric reverse engineering on single and bi-layer designs. *J Eur Opt Soc Rapid Publ* 2013;8(0). https://www.jeos.org/index.php/jeos_rp/article/view/13010.
- [66] Zieger P, Fierz-Schmidhauser R, Weingartner E, Baltensperger U. Effects of relative humidity on aerosol light scattering: results from different European sites. *Atmosph Chem Phys* 2013;13(21):10609–31. <http://www.atmos-chem-phys.net/13/10609/2013/> doi: 10.5194/acp-13-10609-2013.
- [67] Kleinman DA, Spitzer WG. Theory of the optical properties of quartz in the infrared. *Phys Rev* 1962;125:16–30. doi:10.1103/PhysRev.125.16.
- [68] Kitamura R, Pilon L, Jonasz M. Optical constants of silica glass from extreme ultraviolet to far infrared at near room temperature. *Appl Opt* 2007;46(33):8118–33. <http://ao.osa.org/abstract.cfm?URI=ao-46-33-8118> doi: 10.1364/AO.46.008118.
- [69] Huffman D. Pitfalls in calculating scattering by small particles. In: Allamandola LJ, Tielens AGGM, editors. *Interstellar dust*. IAU Symposium, 135; 1989. p. 329.
- [70] Hlavay J, Jonas K, Elek S, Inczey J. Characterization of the particle size and the crystallinity of certain minerals by IR spectrophotometry and other instrumental methods; II, investigations on quartz and feldspar. *Clays Clay Mine* 1978;26(2):139–43. <http://ccm.geoscienceworld.org/content/26/2/139>.
- [71] O'Connor BH, Chang W-J. The amorphous character and particle size distributions of powders produced with the micronizing mill for quantitative x-ray powder diffractometry. *X Ray Spectrom* 1986;15(4):267–70. doi:10.1002/xrs.1300150409.
- [72] Min M, Hovenier JW, de Koter A. Shape effects in scattering and absorption by randomly oriented particles small compared to the wavelength. *A&A* 2003;404(1):35–46. doi:10.1051/0004-6361:20030456.
- [73] Fabian D, Henning T, Jäger C, Mutschke H, Dorschner J, Wehrhan O. Steps toward interstellar silicate mineralogy - vi. dependence of crystalline olivine IR spectra on iron content and particle shape. *A&A* 2001;378(1):228–38. doi:10.1051/0004-6361:20011196.
- [74] Li A, Greenberg JM, Zhao G. Modelling the astronomical silicate features-I. on the spectrum subtraction method. *Month Not R Astronom Soc* 2002;334(4):840–6. doi:10.1046/j.1365-8711.2002.05562.x.
- [75] Pontoppidan K, Fraser H, Dartois E, Thi W, van Dishoeck E, Boogert A, et al. A 3–5 μm VLT spectroscopic survey of embedded young low mass stars I: structure of the CO ice. *Astronomy Astrophys* 2003;408:981–1007. doi:10.1051/0004-6361:20031030.
- [76] Waterman PC. Symmetry, unitarity, and geometry in electromagnetic scattering. *Phys Rev D* 1971;3:825–39. doi:10.1103/PhysRevD.3.825.
- [77] Mishchenko MI, Travis LD, Mackowski DW. T-Matrix computations of light scattering by nonspherical particles: a review. *J Quant Spectrosc Ra-*

- diat Transf 1996;55(5):535–75. <http://www.sciencedirect.com/science/article/pii/S0022407396000027> doi: 10.1016/0022-4073(96)00002-7.
- [78] Nousiainen T, Muñoz O, Lindqvist H, Mauno P, Videen G. Light scattering by large saharan dust particles: comparison of modeling and experimental data for two samples. J Quant Spectrosc Radiat Transf 2011;112(3):420–33. <http://www.sciencedirect.com/science/article/pii/S002240731000364X> doi: 10.1016/j.jqsrt.2010.09.003.
- [79] Nousiainen T, Vermeulen K. Comparison of measured single-scattering matrix of feldspar particles with t-matrix simulations using spheroids. J Quant Spectrosc Radiat Transf 2003;79–80:1031–42. <http://www.sciencedirect.com/science/article/pii/S0022407302003370> doi: 10.1016/S0022-4073(02)00337-0.
- [80] Mishchenko MI, Travis LD. Capabilities and limitations of a current FORTRAN implementation of the T-matrix method for randomly oriented, rotationally symmetric scatterers. J Quant Spectrosc Radiat Transfer 1998;60:309–24. doi:10.1016/S0022-4073(98)00008-9.
- [81] Spitzer WG, Kleinman DA. Infrared lattice bands of quartz. Phys Rev 1961;121:1324–35. doi:10.1103/PhysRev.121.1324.
- [82] Kischkat J, Peters S, Gruska B, Semtsiv M, Chashnikova M, Klinkmüller M, et al. Mid-infrared optical properties of thin films of aluminum oxide, titanium dioxide, silicon dioxide, aluminum nitride, and silicon nitride. Appl Opt 2012;51(28):6789–98. <http://ao.osa.org/abstract.cfm?URI=ao-51-28-6789> doi: 10.1364/AO.51.006789.